

## **Analog Switching Characteristics in TiW/ Al<sub>2</sub>O<sub>3</sub>/ Ta<sub>2</sub>O<sub>5</sub>/ Ta RRAM devices**

Wendong Song, Weijie Wang, Hock Koon Lee, Minghua Li, Victor Yi-Qian Zhuo\*,  
Zhixian Chen, King Jien Chui, Jen-Chieh Liu, I-Ting Wang, Yao Zhu\* and Navab Singh

Institute of Microelectronics, Agency for Science, Technology and Research (A\*STAR),  
Singapore 138634, Singapore,

### **Abstract**

In this letter, we report analog switching characteristics in an analog resistive random access memory device based on TiW/Al<sub>2</sub>O<sub>3</sub>/Ta<sub>2</sub>O<sub>5</sub>/Ta stack. For this device, both oxides were grown by using an atomic layer deposition (ALD) system and the oxygen vacancies were found to exist at the interface of these oxides by using an angle-resolved X-ray Photoelectron Spectroscopy (XPS). The device exhibits analog switching behaviors. Multiple states were achieved by applying 128 consecutive identical pulses of <20  $\mu$ s in duration and stable for at least 10<sup>4</sup> seconds. These characteristics show that the TiW/Al<sub>2</sub>O<sub>3</sub>/Ta<sub>2</sub>O<sub>5</sub>/Ta device is a promising candidate for synaptic application.

---

\* Authors to whom correspondence should be addressed.

Electronic mail: victor-zhuo@ime.a-star.edu.sg; zhuya@ime.a-star.edu.sg

Resistive random access memory (RRAM) has been investigated as the next generation nonvolatile memory due to its simple structure, high speed and low power consumption.<sup>1</sup> Most RRAM studies are focused on digital switching, and as a result, the analog switching characteristics are not sufficiently addressed.<sup>2</sup> Since the analog switching with gradual conductance change exhibits promising features in exploiting artificial synapses for synaptic applications, it is essential to explore the analog switching characteristics of RRAM devices.<sup>3</sup>

Analog RRAM devices can be divided into filamentary and non-filamentary (interfacial) types.<sup>4-11</sup> For filamentary analog RRAM devices based on stacked materials such as TiN/HfO<sub>x</sub>/AlO<sub>x</sub>/Pt,<sup>12</sup> Pt/GeSO/TiN,<sup>13</sup> TiN/TiO<sub>x</sub>/Ta<sub>2</sub>O<sub>5</sub>/TiN,<sup>14</sup> Ti/TiO<sub>2-x</sub>/HfO<sub>2-y</sub>/TiO<sub>2-x</sub>/Au<sup>15</sup> and TiN/HfO<sub>x</sub>/TaO<sub>x</sub>/TiN,<sup>16</sup> the resistive switching is caused by the restore/rupture of a conductive filament or multiple weak filaments in the layered oxide structure.<sup>4</sup> Whereas, for non-filamentary analog RRAM devices based on stacked materials such as Ag/NiO/Pt,<sup>3</sup> Ta/TaO<sub>x</sub>/TiO<sub>2</sub>/Ti,<sup>17</sup> Al/AlO<sub>x</sub>/Ta<sub>2</sub>O<sub>5</sub>/TaO<sub>x</sub>/W<sup>18</sup> and Al/Mo/Pr<sub>0.7</sub>Ca<sub>0.3</sub>MnO<sub>3</sub>/Pt,<sup>19</sup> the resistive switching is induced by the shift of the oxygen ions/vacancies at the oxide/oxide and/or electrode/oxide interfaces, resulting in the modulation of Schottky barrier and/or tunneling barrier.<sup>4</sup> Recent research has demonstrated that the non-filamentary RRAM has advantages over its filamentary counterpart in terms of smaller random telegraph noise (RTN), tighter RTN distribution and lower RTN occurrence rate.<sup>20-21</sup> However, sufficiently long pulses (~ms) are required to shift the oxygen ions/vacancies to modify Schottky and/or tunneling barrier in these non-filamentary analog RRAM devices, which results in slow speed and state instability.<sup>4</sup> Therefore, it is highly desirable to improve analog properties in a non-filamentary analog RRAM device for synaptic applications.

In most analog RRAM devices, at least one oxide is sub-oxide such as TaO<sub>x</sub>, HfO<sub>x</sub>, TiO<sub>x</sub> or AlO<sub>x</sub> and a large number of oxygen vacancies would exist in this oxide layer. In this letter, we

report a non-filamentary analog RRAM device based on TiW/Al<sub>2</sub>O<sub>3</sub>/Ta<sub>2</sub>O<sub>5</sub>/Ta stack. Both oxides are designed and fabricated as full oxides grown by an ALD system. The oxygen vacancies were found to exist at the interface of these oxides by using an angle-resolved XPS. We demonstrated analog switching with fast writing speed and observed multiple states in this device. We studied the conduction mechanism in the different states and discussed the mechanism of analog switching.

The TiW/Al<sub>2</sub>O<sub>3</sub>/Ta<sub>2</sub>O<sub>5</sub>/Ta devices were fabricated on an 8-inch thermal oxide Si wafer. Both the top TiW (30 nm) and bottom Ta (100 nm) electrodes were deposited using the physical vapor deposition method whereas the sandwiched dual metal oxides, 2nm Al<sub>2</sub>O<sub>3</sub> and 4nm Ta<sub>2</sub>O<sub>5</sub> were deposited by an ALD system at 300 °C using Trimethylaluminium (TMA) and Ta[N(C<sub>2</sub>H<sub>5</sub>)<sub>2</sub>NC(CH<sub>3</sub>)<sub>3</sub>] (TBTDET) precursors plus H<sub>2</sub>O as a reactant with 20 and 40 cycles, respectively. After the deposition of these stacked materials, pillar structures of feature sizes ranging from 400nm to 1000nm were patterned using a deep ultraviolet (DUV) lithography system and subsequently etched using an ion beam etch method. The pillars were then passivated with SiO<sub>2</sub> before the formation of top contact openings using the chemical mechanical polishing (CMP) method. The bottom contact openings were then etched through the SiO<sub>2</sub> onto the Ta layer before the formation of contact pads.

The DC I-V curves were measured by a semiconductor characterization system (Keithley 4200-SCS) at room temperature. A Keysight B1500A semiconductor device parameter analyzer with AC signal generation accessory was also employed for pulse measurements of the RRAM device. Transmission electron microscopy (TEM: Tecnai TF20) analysis was carried out to study the microstructures of the RRAM device. The cross-sectional TEM sample was prepared by focused ion beam milling (FIB: DA300) of the device. The angle-resolved XPS (PHI Quantera

SXM Scanning X-ray Microprobe) was used for composition and chemical state analysis. For the XPS, one sample with a Ta<sub>2</sub>O<sub>5</sub> film on a Ta substrate and another sample with Al<sub>2</sub>O<sub>3</sub>/Ta<sub>2</sub>O<sub>5</sub> films on a Ta substrate were prepared by ALD as well as an Al<sub>2</sub>O<sub>3</sub> single crystal substrate were prepared for angle-resolved XPS experiments.

Figure 1(a) exhibits a cross-sectional TEM image of the TiW/Al<sub>2</sub>O<sub>3</sub>/Ta<sub>2</sub>O<sub>5</sub>/Ta device where the stacked structure is clearly observed. The thicknesses of Al<sub>2</sub>O<sub>3</sub> and Ta<sub>2</sub>O<sub>5</sub> are approximately 2nm and 4nm respectively, which is consistent with our design. The chemical states of Al and Ta in aluminum oxide and tantalum oxide thin films were analyzed by angle-resolved XPS. It was found that the sampling depth can be changed by varying the photoelectron take-off angle of  $\theta$ . At  $\theta=10^\circ$ , most of the collected electrons originate from atoms near the surface of the sample. At  $\theta=80^\circ$ , more electrons are collected from atoms deeper in the sample.<sup>22</sup> The normalized Ta4f spectra of tantalum oxide thin film (4 nm) on Ta substrates grown by ALD is presented in Fig. 1(b). It shows the same binding energy positions for Ta4f at different take-off angles from  $10^\circ$  to  $80^\circ$ , which indicates that the signal collected from the electrons originating from atoms near the surface of the film at  $\theta=10^\circ$  is the same as that from atoms deeper in the film at  $\theta=80^\circ$ . The two peaks were found at 26.6eV and 28.4eV for Ta 4f<sub>7/2</sub> and Ta 4f<sub>5/2</sub>, respectively. These correspond to the +5 oxidation state of Ta. It means that the composition of tantalum oxide thin film is Ta<sub>2</sub>O<sub>5</sub>. It is worth noting that two additional peaks attributed to the Ta metal substrate are observed at a high take-off angle of  $80^\circ$  in Fig. 1(b). Figure 1(c) illustrates the normalized Al2p spectra of aluminum oxide thin film (2 nm) on Ta<sub>2</sub>O<sub>5</sub>/Ta where both aluminum oxide and tantalum oxide on a Ta substrate are grown in the same chamber of ALD and also that of Al<sub>2</sub>O<sub>3</sub> single crystal (inset). We can infer that the composition of aluminum oxide thin film as deposited by ALD is Al<sub>2</sub>O<sub>3</sub>. However, the peaks of sub-oxide TaO<sub>x</sub> emerge at lower binding energies as shown in Fig. 1(d) for

the same aluminum oxide thin film as deposited by ALD on Ta<sub>2</sub>O<sub>5</sub>/Ta substrates. The percentage of TaO<sub>x</sub> with respect to Ta<sub>2</sub>O<sub>5</sub> increases with a decrease of take-off angle. This reveals that TaO<sub>x</sub> is generated at the interface of Al<sub>2</sub>O<sub>3</sub>/Ta<sub>2</sub>O<sub>5</sub> during ALD processes. Therefore, oxygen vacancies exist at the interface of ALD deposited Al<sub>2</sub>O<sub>3</sub>/Ta<sub>2</sub>O<sub>5</sub>, unlike the case of as-sputtered TaO<sub>x</sub> and/or AlO<sub>x</sub> in which a large number of oxygen vacancies would exist in the films.<sup>8</sup>

RRAM devices (TiW/Al<sub>2</sub>O<sub>3</sub>/Ta<sub>2</sub>O<sub>5</sub>/Ta) were tested for analog switching characteristics. During the DC measurement, a bias voltage was applied to the top TiW electrode with the bottom Ta electrode grounded. To test the resistive switching property, a positive voltage on the top TiW electrode was applied to induce the SET process which switches the device from high resistance state (HRS) to low resistance state (LRS). A negative voltage on the TiW electrode was applied to induce the RESET process which switches the device from LRS to HRS. It was found that the forming process existed in filamentary-type RRAM was not observed in this device. Figures 2(a) and 2(b) show consecutive DC sweeps in the RESET and SET processes respectively. The conductance increases gradually with consecutive positive voltage sweeps and decreases gradually with consecutive negative voltage sweeps. 100 consecutive positive voltage sweeps for continuously SET was shown in the inset of Fig. 2b. The conductance continuously increases from 0.35 to 17.5 nS (a ratio of 50) at a read voltage of 0.2 V with 100 positive voltage sweeps. Thus, the device exhibits the multiple states and analog switching behaviors.

The analog resistive switching was also carried out by applying voltage pulses. After each repeating pulse, the current was read by using a DC voltage of 0.8V. Figure 2(c) illustrates the potentiation and depression characteristics of the device at different pulse amplitude and duration. The analog switching with short duration (~μs) or fast writing speed was observed in these devices. It was found that higher pulse amplitude and longer pulse duration will result in larger on/off ratio.

As shown in Fig. 2(d), the device conductance was continuously tuned up by applying consecutive identical positive pulses (3.6V, 600ns) and tuned down by applying consecutive identical negative pulses (−3.6V, 20μs). It demonstrated that the conductance gradually changes both for potentiation and depression using pulses of 600ns and 20μs in duration, respectively. Multiple states were achieved by 128 identical programming pulses. We also tested 1000 cycles with 64 identical positive pulses for potentiation and 64 identical negative pulses for depression showing reliable cycling endurance.

Figure 3 displays DC I-V curves at different cell sizes (400nm, 600nm, 800nm and 1000nm). We observed that device current increases with the increase in device cell size. This hints that switching occurs across the entire area. Figure 3(c) exhibits area dependence of the resistance in initial resistance state (IRS) and LRS with a reading voltage of 0.8V after each sweep at 2.5V. In our device, the initial resistance state is HRS. The strong area dependence in both IRS and LRS was obtained, unlike the filamentary RRAM device in which the LRS is insensitive to the device area.<sup>23,24</sup> The resistance in LRS decreases with an increase of the device area supporting a non-filamentary switching mechanism in the device.<sup>18,19,25</sup> To evaluate the memory performance of the device, the retention characteristics was measured at room temperature and 125 °C as shown in Fig. 3(d). All HRS and LRS were stable for at least 10<sup>4</sup> seconds.

DC I-V curves at different SET voltages are shown in Fig. 4(a) and Fig. 4(b). No analog switching was observed at a SET voltage below 1.2 V. Above it, the electrical field is sufficient to induce analog switching. We define this voltage as the threshold voltage for analog switching. It is found that this threshold voltage does not depend on device cell size. The conduction mechanism in the RRAM device of TiW/Al<sub>2</sub>O<sub>3</sub>/Ta<sub>2</sub>O<sub>5</sub>/Ta is explored through the fitting of I–V curves for the positive and negative voltage sweep regions. We found that both space charge limited current and

Fowler-Nordheim tunneling fittings are not good, whereas, we found that both Poole-Frenkel (P-F) emission and Schottky emission fittings are good with the coefficient of determination ( $R^2$ ) larger than 99% as shown in Fig.4. Therefore, both P-F emission and Schottky emission play important roles in the current conduction of the device.<sup>1,3</sup> This is because the vacancies or defects exist at three interfaces ( $\text{Ta}/\text{Ta}_2\text{O}_5$ ,  $\text{Al}_2\text{O}_3/\text{Ta}_2\text{O}_5$  and  $\text{Al}_2\text{O}_3/\text{TiW}$ ) in our devices. The electrons overcome Schottky barrier at metal/oxide interfaces into the conduction band through Schottky emission and escape from their traps into the conduction band through Poole-Frenkel (P-F) emission. We further measured I-V curves at different temperatures from room temperature to 100 K using a superconducting quantum interference device (SQUID) magnetometer (Quantum Design MPMS XL). It was found that the relationship between  $\ln I$  (or  $\ln I/V$ ) and  $1/KT$  is linear where  $K$  is Boltzmann's constant and  $T$  is the temperature, which gives evidence for both conduction mechanisms.

In summary, an analog RRAM device has been designed and fabricated. Bilayer oxides of  $\text{Al}_2\text{O}_3$  and  $\text{Ta}_2\text{O}_5$  deposited by ALD were used in this device and oxygen vacancies were found to exist at the interface of these oxides by an angle-resolved XPS analysis. The resistance in LRS decreases with an increase in the device area. Both Poole-Frenkel (P-F) emission and Schottky emission dominate the current conduction of the device. These suggest that our device is a non-filamentary (interfacial) type where the resistive switching is induced by the shifts of the oxygen ions/vacancies at the oxide/oxide and electrode/oxide interfaces, in which result in the modulation of Schottky barrier and tunneling barrier. This non-filamentary (interfacial) type device shows well-defined bipolar resistive switching without the forming process. It exhibits the multiple states and analog switching behaviors. Multiple states were achieved by 128 applying consecutive identical pulses of 20  $\mu\text{s}$  in duration for depression and 600 ns in duration for potentiation. The

retention of  $10^4$  s for the multiple states was obtained. These characteristics show that TiW/Al<sub>2</sub>O<sub>3</sub>/Ta<sub>2</sub>O<sub>5</sub>/Ta RRAM device is a promising candidate for synaptic applications.

## Acknowledgement

The research is supported by the SERC grant A1687b0033. The authors are grateful to Ping Luo, Mingsheng Zhang and Rong Ji for their support and help with the high resolution TEM and XPS analysis.

## REFERENCES

1. H. S. P. Wong, H.Y. Lee, S. Yu, Y. S. Chen, Y. Wu, P.S. Chen, B. Lee, F. T. Chen, and M.J. Tsai, Proc. IEEE, 100, 1951(2012).
2. B. Long, Y. Li, and R. Jha, IEEE Electron Device Lett., 33, 706(2012).
3. Y. Li, J. Chu, W. Duan, G. Cai, X. Fan, X. Wang, G. Wang, and Y. Pei, ACS Appl. Mater. Interfaces, 10, 24598(2018).
4. J. Woo and S. Yu, IEEE Nanotechnol. Mag., 12, 36(2018).
5. Y. Sun , H. Xu, C. Wang, B. Song , H. Liu, Q. Liu , S. Liu, and Q. Li,” IEEE Electron Device Lett., 39, 1298(2018).
6. Y. Jeong, S. Kim and W. D. Lu, Appl. Phys. Lett. 107, 173105(2015).
7. S. Yu, Proc. IEEE, 106, 260(2018).
8. Z. Wang, M. Yin, T. Zhang, Y. Cai, Y. Wang, Y. Yang and R. Huang, Nanoscale, 8, 14015(2016).



9. J.D. Kim, Y.J. Baek, Y. J. Choi, C. J. Kang, H. H. Lee, H.M. Kim, K.B. Kim, and T.S. Yoon, J. Appl. Phys. 114, 224505(2013).
10. T. Chang, S.H. Jo, K.H. Kim, P. Sheridan, S. Gaba, W. Lu, Appl Phys A, 102, 857(2011).
11. Y.F. Wang, Y.C. Lin, I.T. Wang, T.P. Lin & T.H. Hou, Sci. Rep. 5, 10150(2015).
12. S. Yu, Y. Wu, R. Jeyasingh, D. Kuzum, and H.-S. P. Wong, IEEE Trans. Electron Devices, 58, 2729(2011).
13. W. Zhang, Y. Hu, T.C. Chang, T.M. Tsai, K.C. Chang, H.L. Chen, Y.T. Su, R. Zhang, Y.C. Hung, Y.E. Syu, M.C. Chen, J.C. Zheng, H.C. Lin, and S. M. Sze, IEEE Electron Device Lett., 36, 552(2015).
14. J. Woo, A. Padovani, K. Moon, M. Kwak, L. Larcher, and H. Hwang, IEEE Electron Device Lett., 38,1220(2017).
15. P. Bousoulas, I. Michelakaki, E. Skotadis, M. Tsigkourakos, and D. Tsoukalas, IEEE Trans. Electron Devices, 64, 3151(2017).
16. W. Wu, H. Wu, B. Gao, N. Deng, S. Yu, and H. Qian, IEEE Electron Device Lett., 38, 1019(2017).
17. L. Gao, I.T. Wang, P.Y Chen, S. Vrudhula, J.S Seo, Y. Cao, T.H. Hou and S. Yu, Nanotechnology, 26, 455204(2015).
18. X. Li, H. Wu, B. Gao, W. Wu, D. Wu, N. Deng, J. Cai and H. Qian, Nanotechnology, 27, 305201(2016).
19. K. Moon, A. Fumarola, S. Sidler, J. Jang, P. Narayanan, R. M. Shelby, G. W. Burr, and H. Hwang, J. Electron Devices Soc., 6,146(2018).
20. Z. Chai, P. Freitas, W. Zhang, F. Hatem, J. F. Zhang, J. Marsland, B. Govoreanu, L. Goux and G. S. Kar, IEEE Electron Device Lett., 39 , 1652(2018).

21. J.G. Ma, Z. Chai, W.D Zhang, J.F. Zhang, Z.G. Ji, B. Benbakhti, B. Govoreanu, E. Simoen, L. Goux, A. Belmonte, R. Degraeve, G.S. Kar, M. Jurczak, IEEE Trans. Electron Devices, 65, 970(2018).
22. W. D. Song, J. F. Ying, W. He, V. Y.-Q. Zhuo, R. Ji, H. Q. Xie, S. K. Ng, Serene L. G. Ng, and Y. Jiang, Appl. Phys. Lett. 106, 031602(2015).
23. P. Bousoulas, P. Asenov, I. Karageorgiou, D. Sakellariopoulos, S. Stathopoulos, and D. Tsoukalas, J. Appl. Phys., 120, 154501(2017).
24. F. Nardi, S. Larentis, S. Balatti, D.C. Gilmer, and D. Ielmini, IEEE Trans. Electron Devices, 59, 2461(2012).
25. Y.D.Lin, P.S. Chen, H.Y. Lee, Y.S. Chen, S. Z. Rahaman, K.H. Tsai, C. H. Hsu, W.S. Chen, P.H. Wang, Y.C. King and C. J. Lin, Nanoscale Res. Lett., , 12, 407(2017).

## Figure Captions

Fig. 1 (a) cross-sectional TEM image of the TiW/Al<sub>2</sub>O<sub>3</sub>/Ta<sub>2</sub>O<sub>5</sub>/Ta device, (b) Ta4f spectra of tantalum oxide thin film on Ta substrates, (c) Al2p spectra of aluminum oxide thin film on Ta<sub>2</sub>O<sub>5</sub>/Ta and Al<sub>2</sub>O<sub>3</sub> single crystal, (d) Ta4f spectra of aluminum oxide thin film on Ta<sub>2</sub>O<sub>5</sub>/Ta . The peaks of sub-oxide TaO<sub>x</sub> emerge at lower binding energies and TaO<sub>x</sub> is generated at the interface of Al<sub>2</sub>O<sub>3</sub>/Ta<sub>2</sub>O<sub>5</sub>.

Fig. 2 (a) analog multiple states obtained by identical RESET voltage of -2.5 V for consecutive sweeps, (b) analog multiple states obtained by identical SET voltage of 2.5 V for consecutive sweeps and 100 consecutive positive voltage sweeps for continuously SET listed in the inset,(c) potentiation and depression characteristics of the device at different pulse amplitude and duration, (d) Potentiation and depression in the conductance of the device by identical positive pulses (3.6 V, 600 ns) and identical negative pulses (-3.6 V, 20  $\mu$ s).

Fig. 3 DC I-V curves at different cell sizes (a) 400 and 600 nm, (b) 800 and 1000 nm; (c) area dependence of the resistance in initial resistance state (IRS), low resistance states LRS1 and LRS2 with a reading voltage of 0.8 V; (d) Retention behavior of different resistance states (1-4) from HRS to LRS at room temperature (red lines) and states (5-6) from LRS to HRS at 125 °C (blue lines).

Fig. 4 DC I-V curves at different SET voltages (a) 1.8 V and 2.5 V, (b) 1.2 V and 1.5 V; Poole-Frenkel (P-F) emission fitting of I-V curves for the (c) positive and (d) negative voltage sweep regions. Schottky emission fitting of I-V curves for the (e) positive and (f) negative voltage sweep regions. Temperature dependence of the current at the voltage of 2.5 V shown in the inset of Fig. 4(d) and Fig. 4(f).

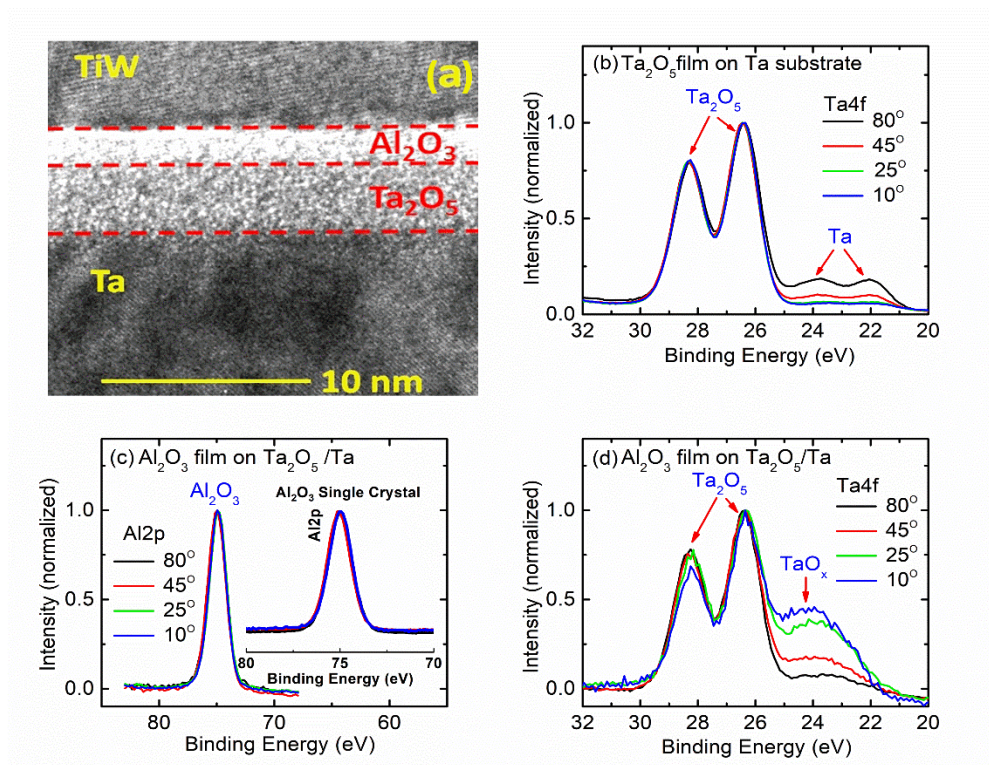


Fig1

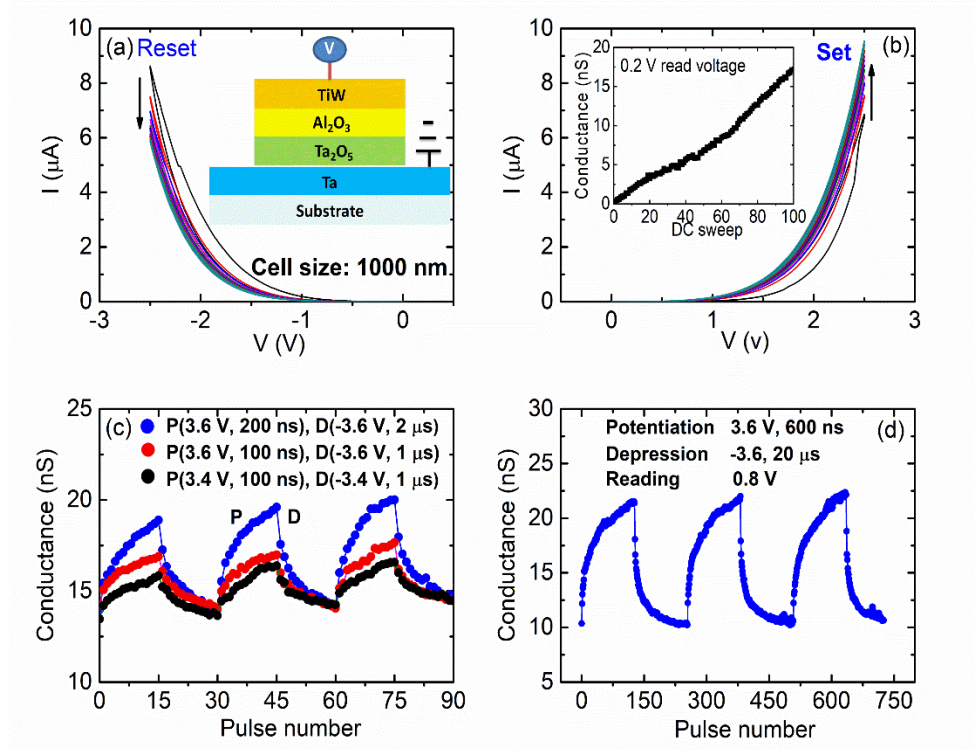


Fig. 2

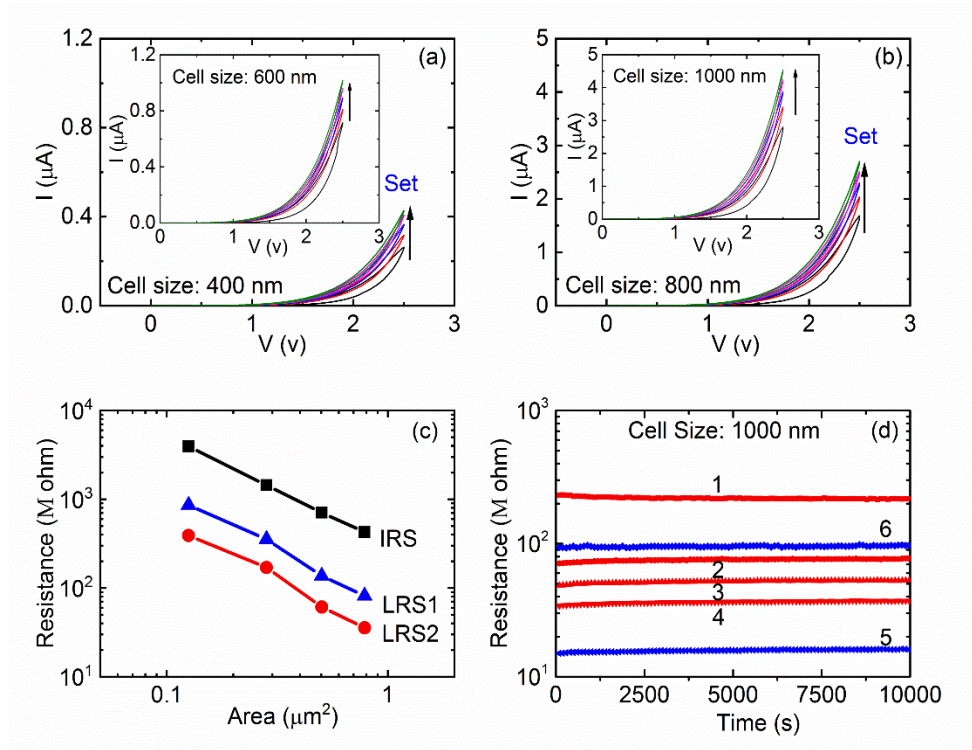


Fig. 3



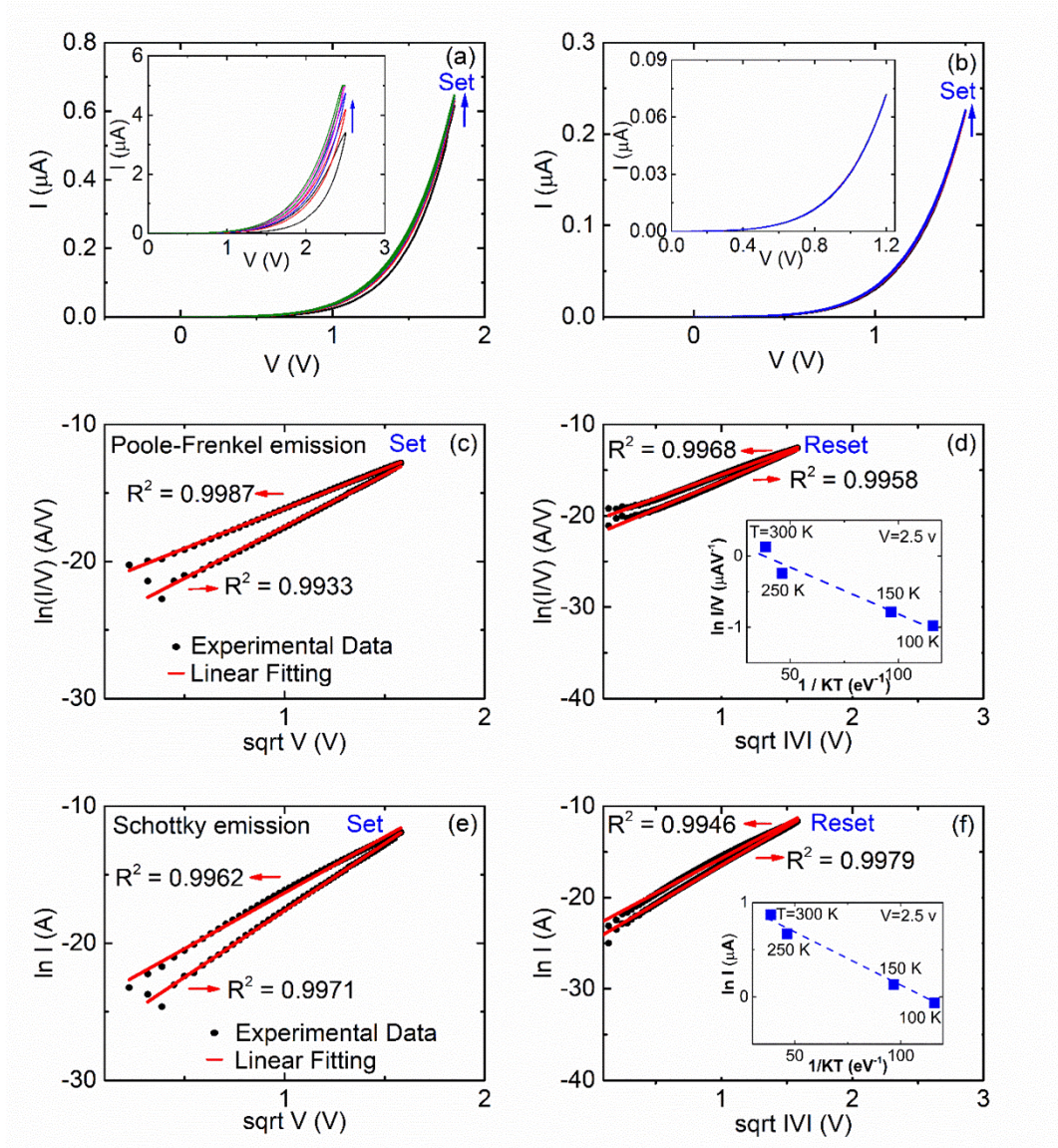


Fig. 4